

Structure-Informed Estimation for Pilot-Limited MIMO Channels via Tensor Decomposition

Alexandre Barbosa de Lima¹

¹Engineering Department, Pontifícia Universidade Católica de São Paulo (PUC-SP), São Paulo, Brazil

Email: ablima@pucsp.br

February 5, 2026

Abstract

Channel estimation in wideband multiple-input multiple-output (MIMO) systems faces fundamental pilot overhead limitations in high-dimensional beyond-5G and sixth-generation (6G) scenarios. This paper presents a hybrid tensor–neural architecture that formulates pilot-limited channel estimation as low-rank tensor completion from sparse observations—a fundamentally different setting from prior tensor methods that assume fully observed received signal tensors. A canonical polyadic (CP) baseline implemented via a projection-based scheme (Tucker completion under partial observations) and Tucker decompositions are compared under varying signal-to-noise ratio (SNR) and scattering conditions: CP performs well for specular channels matching the multipath model, while Tucker provides greater robustness under model mismatch. A lightweight three-dimensional (3D) U-Net learns residual components beyond the low-rank structure, bridging algebraic models and realistic propagation effects. Empirical recovery threshold analysis shows that sample complexity scales approximately with intrinsic model dimensionality $L(N_r + N_t + N_f)$ rather than ambient tensor size $N_r N_t N_f$, where L denotes the number of dominant propagation paths. Experiments on synthetic channels demonstrate 10–20 dB normalized mean-square error (NMSE) improvement over least-squares (LS) and orthogonal matching pursuit (OMP) baselines at 5–10% pilot density, while evaluations on DeepMIMO ray-tracing channels show 24–44% additional NMSE reduction over pure tensor-based methods.

Keywords: MIMO channel estimation, tensor decomposition, structure-informed learning, low-rank recovery, pilot overhead reduction.

1 Introduction

Wideband multiple-input multiple-output (MIMO) systems with large antenna arrays are fundamental enablers of high-capacity wireless links in fifth-generation (5G) and beyond networks. Point-to-point MIMO configurations are particularly relevant for wireless backhaul, fixed wireless access, vehicle-to-infrastructure communications, and satellite feeder links [1, 2]. However, the spectral efficiency gains from spatial multiplexing critically depend on accurate channel state information (CSI), whose acquisition becomes progressively challenging as antenna counts, bandwidth, and mobility increase [3].

Recent advances in radio-frequency (RF) integration have fundamentally altered the architectural landscape of large-array systems. Fully digital transceivers—once considered impractical at millimeter-wave frequencies—are now recognized as scalable and energy-efficient, with commercial deployments already

underway at sub-6 GHz and expected at millimeter-wave (mmWave) frequencies [4]. This architectural shift is further motivated by emerging sixth-generation (6G) use cases such as Integrated Sensing and Communications (ISAC), where fine-grained, per-antenna access to received signals is essential for joint optimization across communication and sensing tasks [5]. The present work focuses on fully digital MIMO orthogonal frequency-division multiplexing (MIMO-OFDM) architectures with direct baseband access to individual antenna-domain channel coefficients¹.

Conventional estimation techniques such as least squares (LS) and linear minimum mean-square error (LMMSE) require pilot resources scaling with channel dimensionality. In wideband MIMO-OFDM systems, the channel comprises $N_r \times N_t \times N_f$ complex coefficients, translating to tens of thousands of unknowns for systems with tens of antennas and hundreds of subcarriers [6, 7]. Deep learning addresses pilot scarcity by learning nonlinear mappings from sparse observations to full reconstructions [8–12], achieving strong performance when training and deployment conditions match. However, these methods typically require large labeled datasets, offer limited interpretability, and generalize poorly under distribution shifts—limitations particularly pronounced in pilot-limited regimes. A fundamental challenge is the limited availability of representative training data: unlike computer vision or natural language processing (NLP), acquiring labeled physical-layer data from operational networks is costly and often impractical [4].

Physics-informed learning mitigates generalization issues by embedding prior knowledge through constraints or regularization [13], often via ray tracing or site-specific geometric models [14, 15]. Although effective in controlled settings, these approaches depend on detailed environmental information and scale poorly across heterogeneous deployments. This paper adopts a complementary perspective: exploiting algebraic structure as a universal physical prior. Rather than encoding propagation physics through explicit geometry, algebraic constraints enforce low rank, separability, and multilinear structure arising from fundamental scattering mechanisms—properties that emerge universally from sparse multipath propagation and array geometry, making them portable across deployment scenarios [1, 2, 7]. In wideband systems, these properties combine into hierarchical spatial–frequency correlations naturally captured by tensor decompositions [16–18].

It is instructive to contrast tensor completion with compressed sensing (CS). CS-based approaches assume sparsity in a predefined angular–delay dictionary and recover coefficients from linear measurements, but are susceptible to basis mismatch in off-grid scenarios. Tensor completion instead exploits low-dimensional multilinear structure—such as low canonical polyadic (CP) or Tucker rank—directly in the native antenna–frequency domain without explicit dictionary construction. These perspectives are complementary: sparsity captures parametric specular structure, while multilinear low-rank models capture broader correlations and offer robustness under richer scattering conditions.

Prior tensor-based channel estimation has demonstrated substantial gains. Zhou et al. [17] formulated mmWave estimation as CP decomposition of a fully observed received signal tensor after RF combining—an overdetermined problem targeting hybrid architectures. Tensor methods have also been applied to MIMO relay systems via nested Tucker decompositions [19] and to time-varying channels under high mobility [20]. However, these formulations assume fully observed tensors and do not address pilot-limited completion.

The present work addresses a complementary scenario: pilot-limited estimation in fully digital systems where only a sparse subset of channel tensor entries is observed. This severely underdetermined inverse problem requires regularization through low-rank tensor completion—a fundamentally different mathematical setting applicable to a broader class of MIMO-OFDM systems [4].

The main contributions are:

1. Hybrid tensor–neural architecture:

A two-stage estimator combining low-rank tensor completion

¹Hybrid beamforming architectures compress spatial information prior to baseband processing, limiting the flexibility required for ISAC. Fully digital transceivers preserve the complete spatial–frequency channel structure, naturally motivating estimation frameworks operating on the full antenna-domain tensor.

with neural residual learning, achieving 24–44% NMSE reduction over pure tensor methods on Deep-MIMO ray-tracing channels.

2. **Tensor completion formulation for pilot-limited MIMO:** Unlike prior methods assuming fully observed tensors [17], the problem is formulated as tensor completion from sparse pilot samples.
3. **Comparative CP versus Tucker analysis:** CP outperforms Tucker at moderate-to-high SNR for specular channels, while Tucker provides greater robustness under model mismatch.
4. **Comprehensive validation:** Evaluation against LS and OMP baselines demonstrates 10–20 dB NMSE improvement at 5–10% pilot density on both synthetic and ray-tracing channels.

The remainder of this paper is organized as follows. Section 2 introduces the system and channel models. Section 3 presents tensor representations and algebraic priors. Section 4 describes the estimation framework. Section 5 presents simulation results. Section 6 concludes the paper.

2 System Model

Throughout this paper, scalars are denoted by lowercase letters (e.g., α), vectors by bold lowercase letters (e.g., \mathbf{a}), matrices by bold uppercase letters (e.g., \mathbf{A}), and tensors by calligraphic letters (e.g., \mathcal{H}). The wideband MIMO channel is represented as a third-order tensor $\mathcal{H} \in \mathbb{C}^{N_r \times N_t \times N_f}$, where N_r , N_t , and N_f denote the number of receive antennas, transmit antennas, and subcarriers, respectively. The k -th entry of a vector \mathbf{w} is denoted by $\mathbf{w}[k]$. The outer product is denoted by \circ , the n -mode product by \times_n , the Frobenius norm by $\|\cdot\|_F$, the Hadamard (element-wise) product by \odot , and the Kronecker product by \otimes . All tensor dimensions and ranks are defined consistently with this convention throughout the paper.

A wideband MIMO–OFDM system is considered, with N_t transmit antennas, N_r receive antennas, and N_f subcarriers. Let $\mathbf{H}[k] \in \mathbb{C}^{N_r \times N_t}$ denote the frequency-domain channel matrix at subcarrier $k \in \{1, \dots, N_f\}$. The received signal is

$$\mathbf{y}[k] = \mathbf{H}[k]\mathbf{x}[k] + \mathbf{n}[k], \quad (1)$$

where $\mathbf{x}[k] \in \mathbb{C}^{N_t}$ is the transmitted signal vector and $\mathbf{n}[k] \sim \mathcal{CN}(\mathbf{0}, \sigma^2 \mathbf{I})$ denotes additive white Gaussian noise [21].

In practical pilot-aided OFDM training, the channel tensor is not directly observed. Pilot symbols yield local linear estimates at the antenna–subcarrier resource elements where pilots are transmitted. Accordingly, we model $\mathcal{P}_\Omega(\mathcal{H})$ as the collection of these pilot-based observations, i.e., noisy samples of the channel entries at the pilot locations. This abstraction reduces the training process to entry-wise sampling of the channel tensor (with noise), which is standard in tensor completion and isolates the impact of pilot sparsity from waveform-specific effects.

2.1 Pilot-Based Channel Estimation

During the training phase, known pilot symbols are transmitted over a subset of resource elements (i, j, k) of the channel tensor, so the channel is observed only at a subset of its coefficients. Stacking the frequency-domain channel matrices $\mathbf{H}[k] \in \mathbb{C}^{N_r \times N_t}$ across all N_f subcarriers yields the wideband MIMO channel represented as a third-order tensor

$$\mathcal{H} \in \mathbb{C}^{N_r \times N_t \times N_f}, \quad (2)$$

whose three modes correspond to receive antennas, transmit antennas, and frequency, respectively.

Pilot-based acquisition provides access only to a subset of tensor entries indexed by

$$\Omega \subset \{1, \dots, N_r\} \times \{1, \dots, N_t\} \times \{1, \dots, N_f\}. \quad (3)$$

The resulting observation model is [17]

$$\mathcal{Y}_\Omega = \mathcal{P}_\Omega(\mathcal{H} + \mathcal{N}) = \mathcal{P}_\Omega(\mathcal{H}) + \mathcal{P}_\Omega(\mathcal{N}), \quad (4)$$

where $\mathcal{P}_\Omega(\cdot)$ denotes the entry-wise sampling operator in (5)

$$[\mathcal{P}_\Omega(\mathcal{H})]_{ijk} = \begin{cases} \mathcal{H}_{ijk}, & \text{if } (i, j, k) \in \Omega, \\ 0, & \text{otherwise,} \end{cases} \quad (5)$$

and \mathcal{N} is i.i.d. complex Gaussian noise. The SNR is defined with respect to the average power of the channel entries at pilot locations (i.e., over Ω), ensuring comparability across different pilot densities. Equivalently, $\mathcal{P}_\Omega(\mathcal{H}) = \mathcal{M} \odot \mathcal{H}$, where $\mathcal{M} \in \{0, 1\}^{N_r \times N_t \times N_f}$ is a binary mask with $[\mathcal{M}]_{ijk} = 1$ if $(i, j, k) \in \Omega$. The noise tensor \mathcal{N} is obtained by stacking the per-subcarrier noise vectors $\mathbf{n}[k]$ across receive antennas and frequency indices, consistently with (1).

The tensor completion formulation models pilot-limited observation as entry-wise sampling over an index set Ω . In the experiments, Ω is generated by a pilot mask with either random sampling, a regular grid, or a comb pattern in frequency. For theoretical discussion this work adopts the standard uniform random sampling model (corresponding to the random mask), while structured masks are treated as deterministic sampling patterns under the same observation model.

When the pilot ratio (ρ) satisfies

$$\rho = \frac{|\Omega|}{N_r N_t N_f} \ll 1, \quad (6)$$

only a small fraction of channel tensor coefficients is directly observed. In this pilot-limited regime, recovering the full channel tensor \mathcal{H} from partial and noisy observations \mathcal{Y}_Ω constitutes a severely ill-posed inverse problem: unknowns vastly exceed measurements, the observation operator is highly rank-deficient, and the solution is non-unique and noise-sensitive [6, 7, 22]. This fundamental limitation motivates incorporating structural priors that exploit intrinsic spatial and spectral correlations of the channel to regularize the estimation problem and enable reliable reconstruction.

2.2 Multipath Channel Model

In sparse scattering environments—such as outdoor deployments with limited reflectors or higher-frequency bands—wireless propagation is typically dominated by a small number of specular paths, leading to low-rank multipath channels [2]. Under this assumption, the frequency-domain channel at subcarrier k admits the geometric representation

$$\mathbf{H}[k] = \sum_{\ell=1}^L \alpha_\ell \mathbf{a}_r(\theta_\ell) \mathbf{a}_t^H(\phi_\ell) e^{-j2\pi k \tau_\ell}, \quad k = 1, \dots, N_f, \quad (7)$$

where L denotes the number of dominant propagation paths, $\alpha_\ell \in \mathbb{C}$ are complex path gains, $\mathbf{a}_r(\theta_\ell)$ and $\mathbf{a}_t(\phi_\ell)$ are receive and transmit array steering vectors associated with angles of arrival and departure, respectively, and $\tau_\ell \in [0, 1)$ represents the normalized propagation delay. The exponential term models frequency-dependent phase rotation induced by path delay across OFDM subcarriers.

Eq. (7) reveals that the wideband channel tensor \mathcal{H} can be expressed as a superposition of rank-one components across spatial and frequency dimensions. Consequently, \mathcal{H} admits an intrinsic CP tensor representation [17, 23], with effective tensor rank governed by the number of dominant propagation paths rather than ambient dimensionality. This physically grounded low-rank structure directly motivates tensor-based channel modeling and underpins the structure-informed estimation framework developed in the sequel.

3 Tensor Representations and Algebraic Priors

This section formalizes how fundamental propagation mechanisms in wideband MIMO channels manifest as intrinsic algebraic structure. Building on the multipath model introduced in Section 2, the channel is represented as a low-dimensional tensor whose multilinear structure reflects sparse specular propagation, array-induced spatial correlations, and frequency coherence due to finite delay spread. CP and Tucker decompositions are introduced as principled parameterizations of this structure, providing physically interpretable and computationally efficient priors for pilot-limited channel estimation. Importantly, the two decompositions embody different physical assumptions and offer complementary trade-offs between model compactness and representational flexibility.

3.1 Channel Tensor Representation

Rather than estimating each frequency-domain channel matrix $\mathbf{H}[k]$ independently, the wideband MIMO channel is modeled as a third-order tensor $\mathcal{H} \in \mathbb{C}^{N_r \times N_t \times N_f}$, whose modes correspond to receive antennas, transmit antennas, and subcarriers, respectively. This tensorial representation explicitly exposes correlations across spatial and spectral dimensions induced by array geometry and propagation physics, which per-subcarrier estimation approaches do not exploit [16, 17]. In time-varying scenarios, an additional temporal mode may be incorporated, yielding a higher-order tensor without altering the underlying algebraic structure.

3.2 Canonical Polyadic Decomposition

The sparse multipath channel model in (7) admits a natural representation in terms of the CP decomposition [23],

$$\mathcal{H} = \sum_{r=1}^R \mathbf{u}_r \circ \mathbf{v}_r \circ \mathbf{w}_r, \quad (8)$$

where $\mathbf{u}_r \in \mathbb{C}^{N_r}$, $\mathbf{v}_r \in \mathbb{C}^{N_t}$, and $\mathbf{w}_r \in \mathbb{C}^{N_f}$ are factor vectors associated with the receive, transmit, and frequency modes, respectively, and R denotes the CP rank.

For channels with L dominant propagation paths, selecting $R = L$ yields a parsimonious and physically interpretable representation, with the correspondence

$$\mathbf{u}_\ell = \alpha_\ell \mathbf{a}_r(\theta_\ell), \quad \mathbf{v}_\ell = \mathbf{a}_t^*(\phi_\ell), \quad [\mathbf{w}_\ell]_k = e^{-j2\pi k \tau_\ell}, \quad (9)$$

where k indexes the subcarrier frequencies. Absorbing the complex gain α_ℓ into the receive-mode factor \mathbf{u}_ℓ is a matter of convention; the gain could equivalently be absorbed into \mathbf{v}_ℓ , into \mathbf{w}_ℓ , or distributed across multiple factors. This scaling ambiguity is intrinsic to the CP decomposition: under the Kruskal uniqueness condition, the CP model is unique only up to permutation and scaling of its rank-one components [23].

This correspondence makes explicit that each rank-one tensor component represents a single physical propagation path, implying that the effective CP rank is governed by the number of dominant paths rather than the ambient channel dimensionality. As a result, CP is particularly well matched to propagation regimes dominated by specular ray-like components, such as millimeter-wave channels around 28 GHz, where a small number of strong paths typically capture most of the channel energy. This property underlies the effectiveness of CP-based models for sparse-channel and large-scale MIMO estimation [17]. It is worth emphasizing that the Kruskal uniqueness condition guarantees factor identifiability up to permutation and scaling, which is sufficient for reliable channel reconstruction. Extracting explicit physical parameters, such as angles of arrival or departure, from the estimated factors would require additional structural constraints—e.g., array calibration or explicit enforcement of Vandermonde structure—beyond the scope of this work, which focuses on CSI reconstruction rather than direct parameter estimation.

In the experiment, Tucker reconstruction is performed via alternating projections, consisting of truncated higher-order singular value decomposition (HOSVD) followed by enforcement of consistency with the observed entries. The baseline labeled ‘‘CP’’ corresponds, by default, to a projection-based variant that uses a stable Tucker-completion step under partial observations and returns the completed tensor; direct masked CP-Alternating Least Squares (ALS) is not used here due to numerical instability in sparse, noisy settings.

3.3 Tucker Decomposition

While CP enforces strict rank-one separability across all modes, a more flexible multilinear representation is provided by the Tucker decomposition [24],

$$\mathcal{H} = \mathcal{G} \times_1 \mathbf{U}_r \times_2 \mathbf{U}_t \times_3 \mathbf{U}_f, \quad (10)$$

where $\mathcal{G} \in \mathbb{C}^{R_r \times R_t \times R_f}$ is a low-dimensional core tensor, and $\mathbf{U}_r \in \mathbb{C}^{N_r \times R_r}$, $\mathbf{U}_t \in \mathbb{C}^{N_t \times R_t}$, and $\mathbf{U}_f \in \mathbb{C}^{N_f \times R_f}$ are factor matrices defining low-dimensional subspaces along each mode.

Tucker generalizes CP, which is recovered when the core tensor \mathcal{G} is superdiagonal with $R_r = R_t = R_f$, by relaxing strict separability across modes. The core tensor captures inter-mode interactions that cannot be expressed as independent rank-one components, enabling representation of richer spatial–spectral correlations. From a physical perspective, this flexibility allows Tucker models to capture clustered multipath and moderately diffuse scattering, where multiple rays share correlated angular and delay characteristics. The multilinear ranks (R_r, R_t, R_f) thus control a trade-off between compression and fidelity: smaller ranks yield stronger dimensionality reduction, while larger ranks enable finer modeling of scattering richness and model mismatch.

3.4 Algebraic Priors from Propagation Physics

The tensor decompositions introduced above encode algebraic properties that directly reflect the physical mechanisms governing channel formation:

- **Low rank**, reflecting the presence of a limited number of dominant propagation paths;
- **Structured factor matrices**, capturing array-induced spatial correlations (e.g., approximately Van-dermonde structure in uniform linear arrays);
- **Frequency smoothness**, arising from finite delay spread and limited coherence bandwidth.

The low-rank property has been extensively exploited through matrix completion and matrix sensing formulations for mmWave and terahertz (THz) systems [25], complementing the tensor-based approach adopted in this work. Unlike geometric priors that rely on site-specific environmental descriptions or ray-tracing information, these algebraic constraints arise intrinsically from propagation physics and array structure, and therefore persist across diverse deployment scenarios. As a result, tensor representations provide robust, interpretable, and physically grounded priors for pilot-limited channel estimation, consistent with prior tensor-based formulations in wireless communications [17].

4 Structure-Informed Learning Framework

This section presents the proposed structure-informed learning framework for pilot-limited MIMO channel estimation. The framework is designed to explicitly combine algebraic priors induced by propagation physics with data-driven residual learning in a unified estimation pipeline. A low-rank tensor completion stage first enforces intrinsic multilinear structure arising from sparse multipath propagation, array geometry,

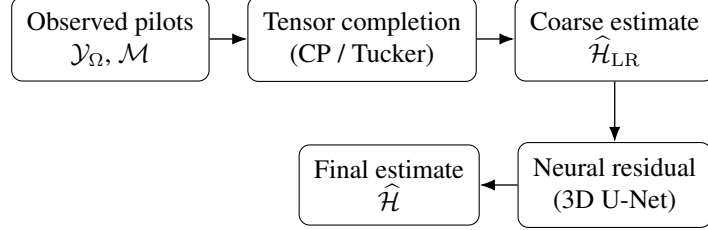


Figure 1: Tensor-NN framework: low-rank tensor completion produces a coarse estimate, refined by a 3D U-Net that learns residual components.

and frequency coherence, yielding a physically consistent coarse channel estimate. A lightweight neural network is then employed to learn residual components that are not captured by the idealized low-rank model, such as diffuse scattering effects, hardware non-idealities, and model mismatch. By decoupling structure enforcement from residual learning, the proposed approach achieves improved robustness and generalization in realistic pilot-limited regimes while retaining interpretability and computational efficiency. Fig. 1 illustrates the proposed two-stage estimation pipeline.

4.1 Problem Formulation

Given sparse pilot observations

$$\mathcal{Y}_\Omega = \mathcal{P}_\Omega(\mathcal{H} + \mathcal{N}) = \mathcal{P}_\Omega(\mathcal{H}) + \mathcal{P}_\Omega(\mathcal{N}), \quad (11)$$

the goal is to estimate the unknown channel tensor \mathcal{H} from incomplete and noisy measurements. This is posed as

$$\widehat{\mathcal{H}} = \arg \min_{\mathcal{H}} \|\mathcal{P}_\Omega(\mathcal{H}) - \mathcal{Y}_\Omega\|_F^2, \quad (12)$$

where $\mathcal{P}_\Omega(\cdot)$ denotes projection onto the observed index set Ω and \mathcal{N} is i.i.d. complex Gaussian noise.

4.2 Tensor Completion via Alternating Projection

Low-rank structure is enforced via an alternating projection scheme that iterates between: (i) a low-rank projection, computed using truncated HOSVD for Tucker models [24]; and (ii) a data-consistency projection, which enforces agreement with the observed pilot samples. For the baseline labeled ‘‘CP’’, the default implementation does not run masked CP alternating least squares (CP-ALS); instead, it uses a stable Tucker-completion step under partial observations and returns the completed tensor. A weighted CP-ALS formulation is implemented but not used by default due to numerical instability in sparse, noisy settings. The resulting estimate satisfies both the algebraic low-rank constraint and consistency with the observed data.

While low-rank tensor models capture the dominant physical structure induced by sparse multipath propagation, they inevitably rely on idealized assumptions that may be violated in practice. In realistic systems, effects such as diffuse scattering, clustered multipath, hardware impairments, and calibration errors introduce structured deviations that cannot be fully represented by CP or Tucker models alone. To address this limitation, the proposed framework augments algebraic tensor completion with a lightweight neural residual learning stage. Importantly, the neural network does not merely perform noise suppression; instead, it learns systematic residual components arising from model mismatch, complementing the physics-inspired tensor model rather than replacing it. This hybrid design places the proposed method within the class of model-aided or physics-informed learning approaches, where algebraic structure provides the primary

Algorithm 1 Tucker Completion via Alternating Projection

Input: Observed tensor \mathcal{Y} , mask \mathcal{M} , ranks (R_r, R_t, R_f) , max iterations T , tolerance ϵ

Output: Completed tensor $\widehat{\mathcal{H}}$

$\mathcal{X}^{(0)} \leftarrow \mathcal{Y}$ {Zero-fill unobserved entries}

for $t = 1, \dots, T$ **do**

Low-rank projection:

$\widehat{\mathcal{X}} \leftarrow \text{HOSVD}_{\text{trunc}}(\mathcal{X}^{(t-1)}, R_r, R_t, R_f)$

Data-consistency projection:

$\mathcal{X} \leftarrow \mathcal{M} \odot \mathcal{Y} + (1 - \mathcal{M}) \odot \widehat{\mathcal{X}}$

Convergence check:

$\delta^{(t)} \leftarrow \frac{\|(\mathcal{X} - \mathcal{X}^{(t-1)}) \odot \mathcal{M}\|_F}{\|\mathcal{Y} \odot \mathcal{M}\|_F + \epsilon}$

if $\delta^{(t)} < \epsilon$ **then**

break

end if

$\mathcal{X}^{(t)} \leftarrow \widehat{\mathcal{X}}$

end for

return $\widehat{\mathcal{H}} \leftarrow \widehat{\mathcal{X}}$

inductive bias and data-driven learning is restricted to correcting non-idealities beyond the expressive power of the underlying mathematical model.

Algorithm 1 details the Tucker completion procedure. Let \mathcal{Y} denote the observed tensor (with unobserved entries set to zero) and let $\mathcal{M} \in \{0, 1\}^{N_r \times N_t \times N_f}$ be the binary mask indicating observed entries ($[\mathcal{M}]_{ijk} = 1$ if $(i, j, k) \in \Omega$). The algorithm seeks a tensor $\widehat{\mathcal{H}}$ of multilinear rank (R_r, R_t, R_f) consistent with the observations.

Stopping criteria Iteration terminates when either: (i) the relative change in observed entries falls below tolerance ϵ , or (ii) the maximum number of iterations T is reached. In all experiments, $\epsilon = 10^{-6}$ and $T = 20$ unless otherwise specified.

Convergence properties Alternating projection for Tucker completion is a block coordinate descent method on a non-convex feasibility problem and typically converges to a stationary point under mild conditions [26]. Global optimality is not guaranteed due to non-convexity of the low-rank constraint. For CP-ALS, the landscape is similarly non-convex, and the algorithm may converge to local minima. Multiple random initializations refer to different initial factor matrices generated deterministically from a fixed base seed.

Rank selection The multilinear ranks (R_r, R_t, R_f) for Tucker and the CP rank R are assumed known or estimated a priori. In practice, rank selection can be performed via model-order criteria such as minimum description length (MDL) or Akaike information criterion (AIC) applied to singular values of tensor unfoldings [23]. For synthetic experiments, ranks are set to match the number of propagation paths ($L = 5$). For DeepMIMO channels, where effective rank is empirical and environment-dependent, ranks are chosen conservatively based on singular value analysis of representative channel realizations. When assumed rank underestimates true channel complexity, the residual $\Delta\mathcal{H} = \mathcal{H} - \mathcal{H}_{\text{LR}}$ increases; the neural residual component is designed to compensate for such model mismatch, as demonstrated in Experiment 5.4.

4.3 Computational Complexity

For CP decomposition with rank R , the number of parameters scales as $\mathcal{O}(R(N_r+N_t+N_f))$, compared with $\mathcal{O}(N_r N_t N_f)$ for unstructured estimation [23]. For typical dimensions ($N_r = N_t = 32$, $N_f = 128$, $R = 5$), this corresponds to approximately $2,000\times$ reduction in degrees of freedom. This substantial complexity reduction explains the effectiveness and scalability of structure-informed estimation in pilot-limited MIMO systems, consistent with prior observations [17].

4.4 Hybrid Tensor–Neural Extension

Although tensor decompositions capture dominant low-dimensional structure induced by sparse multipath propagation, residual errors arise from diffuse scattering, hardware impairments, or model mismatch. To account for these effects, the channel is modeled as

$$\mathcal{H} = \mathcal{T}(\theta) + \Delta\mathcal{H}_{\text{NN}}(\phi), \quad (13)$$

where $\mathcal{T}(\theta)$ denotes a low-rank tensor component and $\Delta\mathcal{H}_{\text{NN}}(\phi)$ a lightweight neural residual. Learning is thus restricted to a correction term rather than the full channel, reducing sample complexity, mitigating overfitting, and improving generalization.

Estimation proceeds in two stages. First, the structured component $\mathcal{T}(\theta)$ is obtained by solving the rank-constrained problem

$$\min_{\mathcal{T}} \|\mathcal{Y}_{\Omega} - \mathcal{P}_{\Omega}(\mathcal{T})\|_F^2 \quad \text{subject to fixed Tucker or CP rank}, \quad (14)$$

via truncated HOSVD with alternating projections for Tucker. Second, the neural network learns the residual by minimizing the supervised mean-squared error (MSE) between predicted and true residuals,

$$\mathcal{L}_{\text{NN}}(\phi) = \|\Delta\mathcal{H}_{\text{NN}}(\phi) - (\mathcal{H} - \mathcal{H}_{\text{LR}})\|_F^2, \quad (15)$$

where \mathcal{H}_{LR} is the low-rank reconstruction and \mathcal{H} the ground-truth channel. This two-stage approach aligns with model-driven and algorithm-unrolling paradigms in signal processing [27–29].

4.4.1 Neural Architecture and Training

The residual term $\Delta\mathcal{H}_{\text{NN}}$ is modeled using a lightweight three-dimensional U-Net architecture [30], denoted Residual3DUNet, specifically designed for residual prediction. The network operates directly on the spatial–frequency channel tensor and exploits encoder–decoder symmetry with skip connections to combine global context and local detail while maintaining a limited parameter count. Table 1 summarizes the layer-by-layer architecture, including channel dimensions and convolutional parameters.

The input consists of the observed tensor \mathcal{Y}_{Ω} represented by separate real and imaginary channels, yielding $C_{\text{in}} = 2$ input channels, optionally augmented with a binary pilot mask ($C_{\text{in}} = 3$). A single encoder–decoder level is employed. The base channel width is denoted by C , with $C = 16$ in all experiments unless otherwise stated.

The encoder applies two $3 \times 3 \times 3$ convolutional layers with padding 1, each followed by ReLU activation, and performs downsampling via a $2 \times 2 \times 2$ strided convolution doubling the channel dimension. The second encoder block begins with ReLU, followed by a $3 \times 3 \times 3$ convolution and another ReLU. The decoder mirrors this structure using transposed convolution for upsampling, concatenation with corresponding encoder features through a skip connection, and two $3 \times 3 \times 3$ convolutions with ReLU activations. The final layer projects features back to the input channel dimension, producing the residual estimate $\widehat{\mathcal{R}}$. When

Table 1: Residual3DUNet architecture for neural residual learning.

Stage	Operation	Channels
Input	—	C_{in}
Encoder-1	Conv3D + ReLU ($3^3/1$)	$C_{\text{in}} \rightarrow C$
	Conv3D + ReLU ($3^3/1$)	$C \rightarrow C$
Downsample	Conv3D ($2^3/2$)	$C \rightarrow 2C$
Encoder-2	ReLU \rightarrow Conv3D \rightarrow ReLU ($3^3/1$)	$2C \rightarrow 2C$
Upsample	ConvTranspose3D ($2^3/2$)	$2C \rightarrow C$
Decoder-1	Concat + ReLU \rightarrow Conv3D + ReLU ($3^3/1$)	$2C \rightarrow C$
Output	Conv3D ($3^3/1$)	$C \rightarrow C_{\text{in}}$

Notation: k^3/s denotes kernel size $k \times k \times k$ with stride s . Base width $C = 16$.

necessary, trilinear interpolation aligns tensor dimensions prior to skip-connection concatenation. No batch normalization, dropout, or other explicit regularization layers are employed.

The reconstructed channel is obtained as

$$\widehat{\mathcal{H}} = \mathcal{H}_{\text{LR}} + \widehat{\mathcal{R}}, \quad (16)$$

where \mathcal{H}_{LR} denotes the low-rank tensor approximation. The resulting network contains approximately 50k trainable parameters.

Training uses the Adam optimizer [31] with fixed learning rate 10^{-3} and batch size 2 (unless otherwise stated). No learning-rate decay or warm-up is used. Early stopping is applied only to the ResNet baseline and is disabled by default; the hybrid Tensor–NN is trained for a fixed number of epochs.

Training details All neural networks are trained using the Adam optimizer with fixed learning rate 10^{-3} and no learning-rate decay or warm-up. Network weights are initialized using PyTorch default initialization schemes, corresponding to Kaiming/He uniform initialization for convolutional and transposed convolutional layers, with biases initialized to zero when present [32].

No explicit data augmentation is applied. Training variability is provided by random channel generation and, when enabled, by sampling pilot ratios and SNR values over predefined ranges (multi-pilot and multi-SNR training). For the proposed hybrid Tensor–NN model, training is performed for a fixed number of epochs without early stopping.

4.4.2 Residual Structure and Architectural Rationale

After low-rank tensor reconstruction, the residual $\Delta\mathcal{H} = \mathcal{H} - \mathcal{H}_{\text{LR}}$ exhibits two dominant characteristics: (i) spatial and spectral smoothness induced by bandlimited propagation and finite delay spread, and (ii) localized components arising from diffuse scattering, hardware impairments, and rank mismatch. This structure naturally spans multiple spatial and frequency scales.

The U-Net architecture is well matched to this residual structure: its encoder captures coarse global context through progressive downsampling, while skip connections preserve fine-scale localized information. This design enables efficient reconstruction of multi-scale residual patterns with a small parameter budget, a property proven effective in inverse problems and denoising tasks involving structured residuals.

5 Simulation Results

This section evaluates pilot-limited wideband MIMO channel estimation under synthetic and ray-tracing-based propagation models. The goal is to quantify how intrinsic tensor structure—in particular, low multilinear rank induced by sparse scattering—enables reliable reconstruction of the wideband channel tensor \mathcal{H} from noisy and incomplete pilot observations [17].

5.1 Setup

For synthetic experiments, the wideband channel is represented as a third-order tensor $\mathcal{H} \in \mathbb{C}^{N_r \times N_t \times N_f}$ with $N_r = N_t = 32$ antennas and $N_f = 128$ subcarriers, generated according to the multipath model in (7) with L dominant paths. Angles satisfy $\theta_\ell, \phi_\ell \sim \mathcal{U}[-\pi/2, \pi/2]$ (angular spread 180°), complex gains α_ℓ are drawn i.i.d. from $\mathcal{CN}(0, 1)$ and normalized to unit total power, and normalized delays satisfy $\tau_\ell \sim \mathcal{U}[0, 1]$. Uniform linear arrays (ULA) with half-wavelength spacing are used at both ends [2, 7]. Pilot acquisition is modeled as entry-wise random sampling over an index set Ω with pilot ratio $|\Omega|/(N_r N_t N_f)$ [26, 33]. Additive white Gaussian noise (AWGN) is applied only to observed entries, and SNR is defined with respect to the average power of observed coefficients.

The following estimators are compared:

- **LS** (zero-fill): baseline estimator setting unobserved entries to zero;
- **OMP**: orthogonal matching pursuit with Kronecker ULA steering dictionary (Rx/Tx), applied independently per subcarrier [7];
- **Tucker**: completion via alternating projection between truncated HOSVD with multilinear ranks (R_r, R_t, R_f) and data-consistency enforcement on Ω [24, 26];
- **CP**: rank- R CP decomposition using Tucker completion as low-rank proxy, with data-consistency projection [23];
- **Tensor-NN**: proposed hybrid architecture combining Tucker completion with lightweight 3D U-Net for residual learning.

Performance is measured by normalized mean-squared error (NMSE),

$$\text{NMSE} = \frac{\|\hat{\mathcal{H}} - \mathcal{H}\|_F^2}{\|\mathcal{H}\|_F^2}, \quad (17)$$

averaged over Monte Carlo (MC) realizations. Table 2 summarizes experiment settings.

5.1.1 DeepMIMO Dataset

To assess the proposed framework under realistic propagation conditions, ray-tracing-based channels are taken from the DeepMIMO dataset [34]. Experiments use the ASU_Campus_3p5 scenario (DeepMIMO v4 pre-release), generated with the Remcom Wireless InSite ray tracer. This scenario models an outdoor campus environment at 3.5 GHz with dense building geometry and heterogeneous scattering objects, providing a substantially more challenging testbed than idealized sparse multipath models. Detailed ray-tracing parameters (path depth, reflections, diffractions) are defined by the DeepMIMO dataset configuration and documented in [34].

Table 2: Simulation parameters.

Parameter	Exp. 1	Exp. 2	Exp. 3
Sweep variable	Pilot ratio	SNR	Pilot ratio
Pilot ratio	2–20%	8%	2–20%
SNR (dB)	10	–5 to 20	10
L paths	5	5	5
$N_r \times N_t \times N_f$	$32 \times 32 \times 128$	$32 \times 32 \times 128$	$16 \times 32 \times 64$
Bandwidth	—	—	50 MHz
Tucker ranks	(4, 4, 6)	(5, 5, 6)	(4, 4, 8)
CP rank R	—	5	5
Dataset	Synthetic	Synthetic	DeepMIMO
MC runs	500	500	500

Point-to-point MIMO-OFDM channels are constructed using ULAs with $N_r = 16$ receive antennas, $N_t = 32$ transmit antennas, and $N_f = 64$ subcarriers over 50 MHz bandwidth. Channels are taken directly from DeepMIMO without path truncation and normalized to unit average power; low-rank structure is therefore empirical rather than enforced by construction.

Training and test sets are defined by random subsampling of user positions with fixed seeds for reproducibility. This partitioning does not enforce explicit geographic separation between training and test locations; evaluating spatial generalization under strict geographic partitioning remains a direction for future work.

5.2 Experiment 1: Tensor Completion under Pilot Scarcity

Fig. 2 evaluates NMSE as a function of pilot ratio at $\text{SNR} = 10$ dB with $L = 5$ paths. This experiment highlights the central contribution: tensor completion yields meaningful reconstruction gains under severe pilot undersampling.

LS yields NMSE near unity across all pilot ratios, confirming that naive zero-filling cannot recover channel structure under sparse sampling. OMP achieves moderate gains at higher pilot ratios but exhibits a performance floor due to dictionary mismatch and per-subcarrier processing that does not exploit frequency-domain correlations.

In contrast, Tucker completion exploits low-rank structure across all three tensor modes and achieves substantial gains even at very low pilot densities (4–6%), with NMSE improving monotonically as more pilots become available. At 10% pilots, Tucker attains approximately one order of magnitude improvement over LS. These results demonstrate that algebraic tensor priors effectively regularize the ill-posed inverse problem arising from pilot-limited observation.

5.3 Experiment 2: CP versus Tucker Decomposition

Fig. 3 compares Tucker and CP as a function of SNR at 8% pilot ratio. This experiment addresses the practical question of decomposition selection based on channel characteristics.

Both tensor methods substantially outperform LS and OMP across all SNR values. At low SNR (–5 and 0 dB), the two methods are comparable, with CP slightly worse (sub-1 dB difference). As SNR increases, CP progressively outperforms Tucker; at $\text{SNR} = 20$ dB, CP achieves about a 3.6 dB NMSE advantage.

This behavior is consistent with the synthetic channel model in (7), which is a sum of L rank-one components. CP provides a tighter parameterization when the channel matches this specular multipath

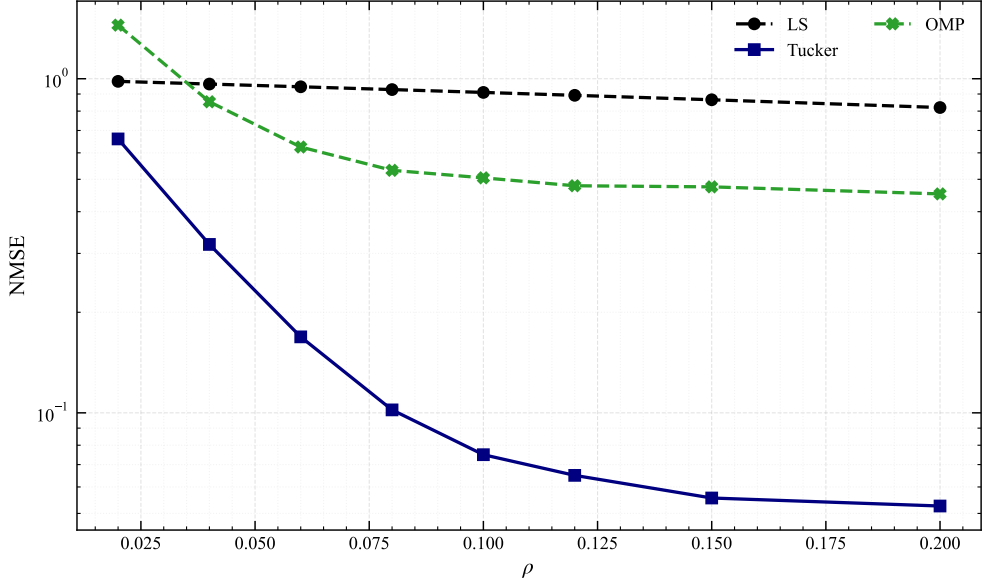


Figure 2: NMSE versus pilot ratio for synthetic channels (SNR = 10 dB, $L = 5$ paths, Tucker ranks (4, 4, 6), 500 MC runs). Tucker completion improves over LS by $\sim 2\text{--}12$ dB across the sweep, exceeding 10 dB for pilot ratios ≥ 0.10 , and it outperforms OMP at all pilot ratios.

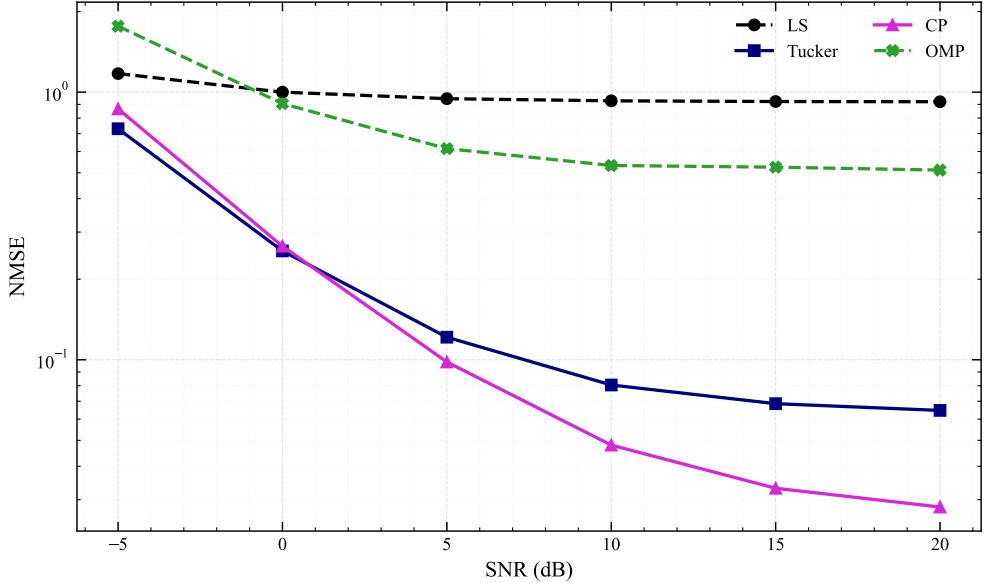


Figure 3: Tucker versus CP as a function of SNR ($\rho = 8\%$, $L = 5$ paths, Tucker ranks (5, 5, 6), CP rank $R = 5$, 500 MC runs). CP performs better than Tucker at moderate-to-high SNR for specular channels consistent with the multipath model.

structure, whereas Tucker introduces additional degrees of freedom through its core tensor. Under model mismatch (e.g., richer scattering or non-ideal effects, as in DeepMIMO), Tucker's flexibility can become advantageous.

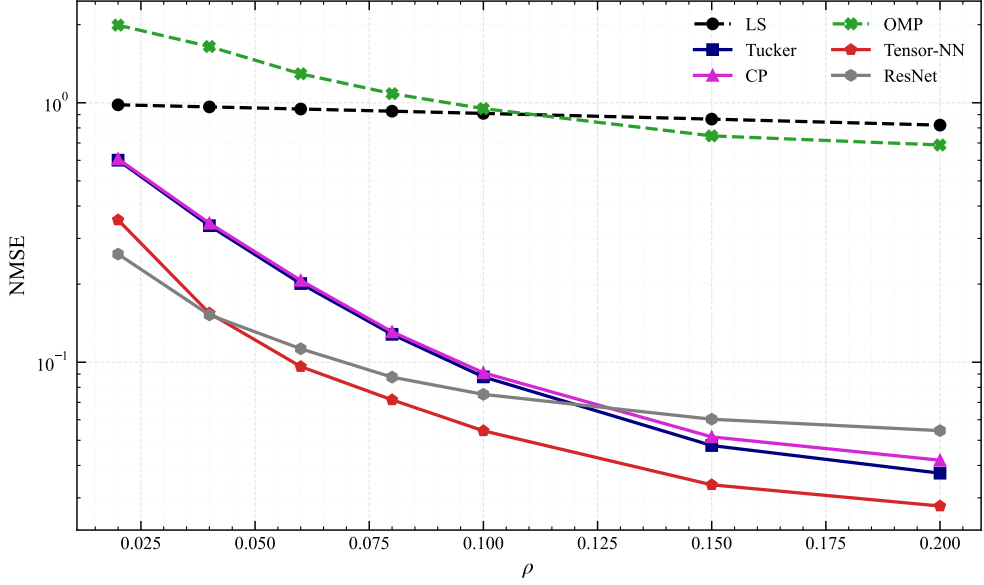


Figure 4: Performance on DeepMIMO ray-tracing channels (ASU_Campus_3p5 scenario, SNR = 10 dB) versus pilot ratio. A purely data-driven ResNet baseline is included for reference. Tensor-NN outperforms Tucker and CP and surpasses ResNet for pilot ratios $\rho \geq 0.04$.

5.4 Experiment 3: Hybrid Tensor–Neural Estimation on DeepMIMO

Fig. 4 evaluates the complete framework on ray-tracing-based DeepMIMO channels at SNR = 10 dB. These channels exhibit higher effective rank due to diffuse scattering and environment-specific propagation characteristics not captured by the idealized model in (7).

Pure tensor methods (Tucker and CP) continue to outperform LS on DeepMIMO channels, but the performance gap relative to synthetic channels narrows due to model mismatch. A purely data-driven ResNet baseline (convolutional neural network (CNN)) is also included [35–37]. The ResNet is a 3D architecture operating on the real/imaginary channels of the observation and the pilot mask (3-channel input), with a $3 \times 3 \times 3$ Conv3D stem, followed by 4 residual blocks (each with two $3 \times 3 \times 3$ Conv3D layers and ReLU), and a final $3 \times 3 \times 3$ Conv3D to predict the 2-channel complex output (base channels = 32).

Tensor-NN consistently outperforms pure tensor methods across all pilot ratios. At 8% pilots, Tensor-NN achieves NMSE ≈ 0.072 compared to ≈ 0.128 (Tucker) and ≈ 0.131 (CP), representing approximately 44% improvement; the ResNet baseline yields NMSE ≈ 0.088 at the same pilot density. Tensor-NN overtakes ResNet from $\rho \geq 0.04$ and maintains a clear gap thereafter. At 20% pilots, Tensor-NN achieves NMSE ≈ 0.028 versus ≈ 0.037 (Tucker), a 24% gain, while ResNet attains ≈ 0.054 .

ResNet training methodology The ResNet baseline is trained offline on paired $(\mathcal{H}, \mathcal{Y}_\Omega)$ samples. Inputs are formed by stacking the real and imaginary parts of the noisy pilot observations together with the binary pilot mask (3-channel input), and the network outputs the real/imaginary channels of \mathcal{H} . Training minimizes the mean-squared error between the predicted and true channel tensors, using Adam optimization and early stopping. To promote robustness, pilot ratios and SNR are sampled from ranges during training (multi-regime training), and random pilot masks are generated per sample. In the pure ResNet setting, no explicit pilot-consistency term is used (i.e., $\lambda_{\text{pilot}} = 0$). For the DeepMIMO experiment, training uses 1500 samples for training and 300 for validation, base channels = 32, and 4 residual blocks.

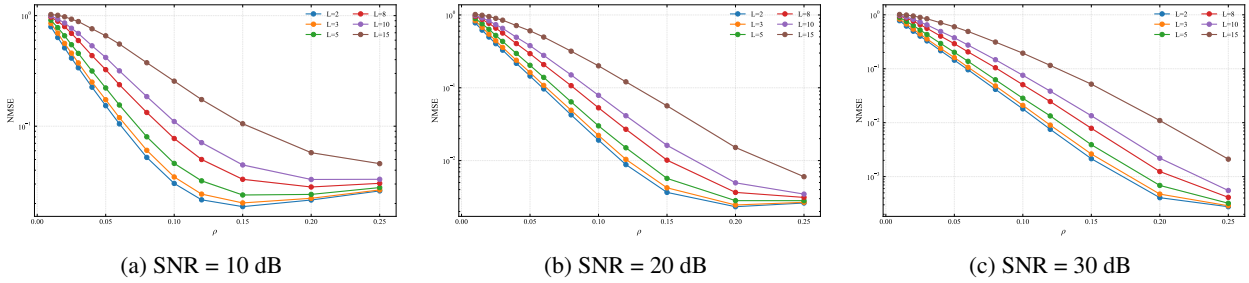


Figure 5: Recovery curves showing NMSE versus pilot ratio ρ for varying number of paths L . Higher SNR sharpens the transition and lowers NMSE within the feasible region.

5.5 Experiment 4: Sample Complexity Analysis

This experiment empirically characterizes the sample complexity of tensor completion by determining the recovery threshold of Tucker reconstruction as a function of the number of observed entries $|\Omega|$. Synthetic channels are generated according to the model in Section 5.1, with $N_r = N_t = 32$ antennas, $N_f = 128$ subcarriers, and $L \in \{2, 3, 5, 8, 10, 15\}$ propagation paths. Pilot ratios are swept from 1% to 25% across 14 sample points, with finer spacing at low pilot ratios (and consequently finer resolution near the transition region). Results are averaged over 100 Monte Carlo realizations, and successful recovery is defined by $\text{NMSE} \leq 10^{-2}$, which determines the empirical threshold $|\Omega|_{\min}$. Following the implementation, Tucker ranks are adapted to L via $(R_r, R_t, R_f) = (L, L, L + 1)$ (capped by N_f).

Recovery curves Fig. 5 plots NMSE versus pilot ratio ρ for each value of L at $\text{SNR} \in \{10, 20, 30\}$ dB. Two consistent trends emerge. First, the recovery transition shifts toward higher pilot densities as L increases, reflecting the growing intrinsic dimensionality of the channel model. Second, higher SNR sharpens the transition and lowers the NMSE once the recovery region is reached. At $\text{SNR} = 10$ dB, no configuration achieves $\text{NMSE} \leq 10^{-2}$ within the tested 25% pilot range, indicating a noise-limited regime where increasing pilot density alone cannot compensate for measurement noise. The curves remain monotonic but do not exhibit a clear threshold within the tested range.

Recovery region heatmaps Fig. 6 visualizes the recovery region in the (L, ρ) plane. The transition band between successful recovery and failure shifts to higher pilot densities as L increases, consistent with the growth in intrinsic model complexity. At $\text{SNR} = 10$ dB, no configuration reaches the $\text{NMSE} \leq 10^{-2}$ threshold within the tested range, indicating a noise-limited regime. For $\text{SNR} \in \{20, 30\}$ dB, the empirical thresholds lie in the 12–25% pilot range and increase monotonically with L . The difference between 20 and 30 dB is modest (with only small reductions of ρ_{\min} for some L), indicating that L dominates the feasibility boundary while higher SNR mainly sharpens the transition and lowers NMSE within the feasible region. These heatmaps provide a compact visualization of the feasibility region for reliable channel reconstruction.

Empirical thresholds and oversampling factor Table 3 reports the minimum pilot ratio ρ_{\min} and corresponding observation count $|\Omega|_{\min}$ required to achieve $\text{NMSE} \leq 10^{-2}$. At $\text{SNR} = 10$ dB, no configuration reaches this threshold within the tested range. For $\text{SNR} \in \{20, 30\}$ dB, thresholds lie in the 12–25% pilot range and increase monotonically with L , confirming that sample complexity is dominated by intrinsic channel structure rather than noise level.

To interpret these results, we compare against the heuristic degrees-of-freedom scaling for low-rank

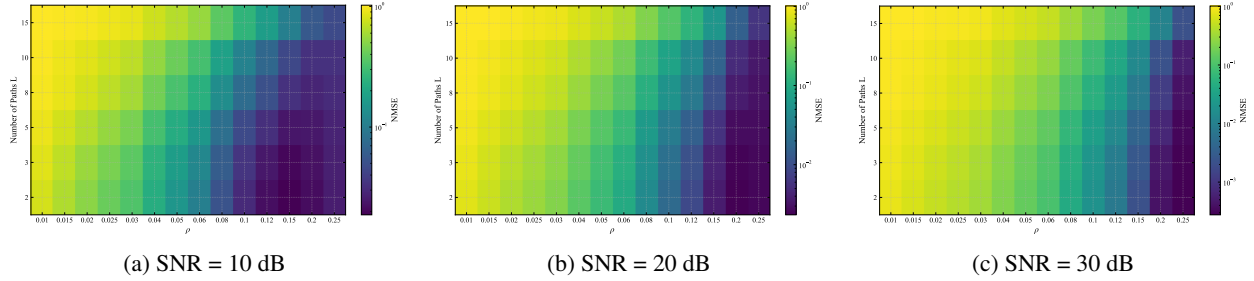


Figure 6: Recovery region heatmaps over (L, ρ) .

Table 3: Empirical thresholds for $\text{NMSE} \leq 10^{-2}$ and oversampling factor.

SNR (dB)	L	ρ_{\min}	$ \Omega _{\min}$	C
20	2	0.120	15728.6	40.96
20	3	0.150	19660.8	34.13
20	5	0.150	19660.8	20.48
20	8	0.200	26214.4	17.07
20	10	0.200	26214.4	13.65
20	15	0.250	32768.0	11.38
30	2	0.120	15728.6	40.96
30	3	0.120	15728.6	27.31
30	5	0.150	19660.8	20.48
30	8	0.150	19660.8	12.80
30	10	0.200	26214.4	13.65
30	15	0.250	32768.0	11.38

tensor recovery:

$$|\Omega|_{\min} \approx C L (N_r + N_t + N_f), \quad (18)$$

where C denotes the oversampling factor. The rightmost column of Table 3 lists the empirically observed C for each configuration. The measured values ($C \approx 11\text{--}41$) exceed theoretical minima established for incoherent low-rank tensors under idealized conditions [38]. This gap is attributable to three factors: (i) Tucker decomposition introduces additional core tensor parameters absent in CP; (ii) finite-sample effects and interpolation in threshold estimation; and (iii) suboptimality of the alternating projection algorithm under noisy, sparse observations.

We emphasize that the scaling in (18) is CP-inspired and serves here as a qualitative proxy for interpreting recovery thresholds. For Tucker models, the exact degrees of freedom additionally depend on the multilinear ranks (R_r, R_t, R_f) and core tensor size. Nonetheless, the empirical results demonstrate that the minimum observation count scales predominantly with intrinsic channel complexity—captured by the number of dominant propagation paths and effective subspace dimensions—rather than with the ambient tensor size $N_r N_t N_f$.

Fig. 7 compares empirical thresholds against the heuristic bound (18) with $C = 5$. At $\text{SNR} = 10 \text{ dB}$, no empirical thresholds are available within the tested range, so only the bound is shown. Despite the constant-factor gap, empirical $|\Omega|_{\min}$ scales approximately linearly with both L and $(N_r + N_t + N_f)$, confirming that sample complexity is governed by intrinsic model dimensionality rather than ambient tensor size.

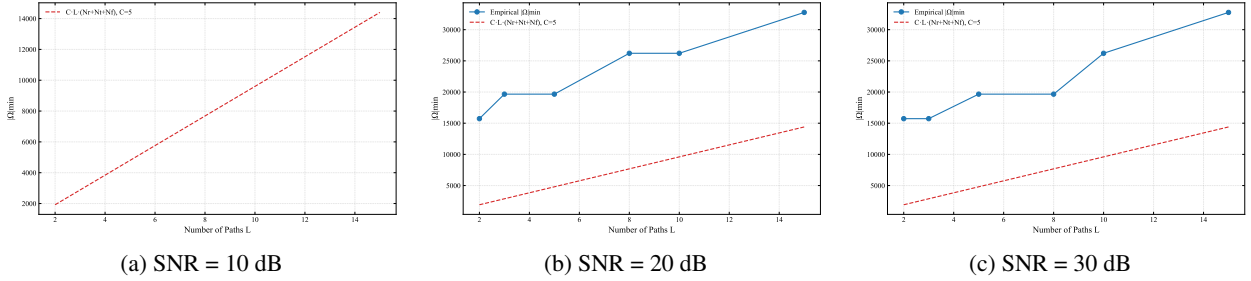


Figure 7: Empirical $|\Omega|_{\min}$ versus the heuristic bound in (18) with $C = 5$ for $\text{SNR} \in \{10, 20, 30\}$ dB.

Table 4: Computational complexity and execution time per channel realization ($N_r = N_t = 32$, $N_f = 128$, pilot ratio = 8%, Apple M3 Pro).

Method	Complexity	Iter.	Time
LS (zero-fill)	$\mathcal{O}(\Omega)$	—	< 1 ms
Tucker	$\mathcal{O}(N_r N_t N_f \cdot R_{\max})$	20	≈ 15 ms
CP	\approx Tucker	30	≈ 25 ms
Tensor-NN	Tucker + $\mathcal{O}(N_r N_t N_f \cdot C^2)$	20+1	≈ 35 ms

Key findings The results confirm the existence of a sharp recovery threshold and yield three principal insights:

1. Successful tensor completion requires a number of observations that scales with intrinsic model complexity rather than ambient tensor dimension.
2. The effective oversampling factor C depends on the decomposition type, SNR, and algorithmic efficiency.
3. At moderate SNR (≥ 20 dB), reliable recovery is achievable with 12–25% pilot density for channels with up to 15 dominant propagation paths.

5.6 Computational Complexity

Table 4 summarizes the computational complexity and measured execution times for each method. The dominant cost in tensor-based approaches is the low-rank projection step. For Tucker completion via truncated HOSVD, each iteration requires $\mathcal{O}(N_r N_t N_f \cdot R_{\max})$ operations, where $R_{\max} = \max(R_r, R_t, R_f)$ denotes the largest multilinear rank. The algorithm converges in 20 iterations for synthetic channels and 30 iterations for DeepMIMO experiments, reflecting the higher effective rank of ray-tracing-based channels.

CP employs Tucker completion as a low-rank proxy followed by data-consistency enforcement, yielding comparable per-iteration cost. The hybrid Tensor-NN method adds a single forward pass through the 3D U-Net (~ 50 k parameters), contributing marginal overhead relative to the tensor completion stage.

All methods achieve execution times below 40 ms per channel realization on an Apple M3 Pro processor, well within the coherence time of typical wireless channels (1–10 ms at pedestrian speeds, 0.1–1 ms at vehicular speeds). The modest overhead of Tensor-NN (~ 20 ms beyond Tucker) is justified by the 24–44% NMSE improvement observed on realistic channels. For deployment on resource-constrained hardware, further acceleration is possible through GPU batching, quantization, or algorithmic simplifications such as reduced iteration count with warm-start initialization.

5.7 Discussion

The experimental results yield three main findings:

1. **Tensor priors enable pilot-limited estimation.** Low-rank Tucker completion improves NMSE by $\sim 2\text{--}12$ dB over LS across the sweep, exceeding 10 dB for $\rho \geq 0.10$, and outperforms OMP at all pilot ratios. The empirical thresholds show that, at moderate-to-high SNR, pilot density is the dominant factor for achieving $\text{NMSE} \leq 10^{-2}$.
2. **Decomposition choice depends on channel structure.** In the synthetic specular model, the CP baseline outperforms Tucker at moderate-to-high SNR (about 3–4 dB at 15–20 dB), while differences are small at low SNR and CP can be slightly worse. In DeepMIMO, Tucker is consistently slightly better than CP, indicating improved robustness under model mismatch. These results suggest CP for channels well approximated by sparse multipath, and Tucker for richer scattering conditions.
3. **Hybrid modeling bridges the model–data gap.** Tensor-NN yields 24–44% additional NMSE reduction on DeepMIMO relative to pure tensor methods and surpasses the ResNet baseline for $\rho \geq 0.04$, indicating that residual learning captures deviations beyond dominant low-rank structure.

5.8 Limitations

Despite the gains reported above, the proposed framework has limitations that merit explicit discussion:

- **Rank selection and sensitivity.** The tensor methods require multilinear ranks (or CP rank) to be specified a priori. In the current implementation, ranks are fixed per experiment and, in the sample-complexity study, are tied to the number of paths via $(R_r, R_t, R_f) = (L, L, L+1)$. Performance can degrade under rank mismatch, and a principled, data-driven rank selection strategy remains necessary for robust deployment.
- **High-mobility and time-varying channels.** The experiments assume quasi-static channels and estimators operate on single snapshots. Rapid mobility, Doppler spread, and temporal correlation are not modeled; extending the framework to spatio-temporal estimation or channel tracking is left for future work.
- **Neural training requirements.** The neural components (Tensor-NN residual and ResNet baselines) are trained offline on paired $(\mathcal{H}, \mathcal{Y}_\Omega)$ data using multi-SNR and multi-pilot regimes. In deployment, this may require representative training data (or synthetic surrogates) and potential fine-tuning to mitigate distribution shift across scenarios, environments, or array configurations.
- **Synchronization and hardware impairments.** The observation model includes only entry-wise sampling with additive Gaussian noise. Effects such as carrier-frequency offset, phase noise, IQ imbalance, nonlinear power amplifiers, low-resolution quantization, and other hardware imperfections are not modeled. Their impact on tensor completion and neural residual learning remains an open question.

5.9 Reproducibility

All experiments were conducted on an Apple M3 Pro laptop (11-core CPU, 14-core GPU, 18 GB unified memory) using Python 3.10 with PyTorch 2.1 and Metal Performance Shaders (MPS) acceleration. A fixed random seed (`base_seed=42`) ensures deterministic channel generation, pilot sampling, and network initialization across all experiments.

The complete codebase—including data generation scripts, training configurations, pretrained model checkpoints, and plotting utilities—is publicly available at:

<https://github.com/alexandreblima/MIMO-TN>

DeepMIMO channels are generated using the official dataset API [34] with configuration files provided in the repository. Researchers can reproduce all figures and tables by executing the provided shell scripts with default parameters.

6 Conclusion

This paper presented a structure-informed framework for pilot-limited MIMO channel estimation that combines low-rank tensor completion with neural residual learning. Unlike prior tensor-based methods that assume fully observed received signal tensors, the proposed approach addresses the fundamentally underdetermined inverse problem arising from sparse pilot observations in fully digital MIMO-OFDM architectures.

The main contributions and findings are summarized as follows:

1. **Tensor completion formulation:** Modeling pilot-limited estimation as low-rank tensor completion yields $\sim 2\text{--}12$ dB NMSE improvement over LS across the sweep (exceeding 10 dB for $\rho \geq 0.10$) and outperforms OMP at all pilot ratios, demonstrating that algebraic structure induced by sparse multipath propagation provides effective regularization under severe undersampling.
2. **Decomposition selection:** In the synthetic specular model, the CP baseline outperforms Tucker by about 3–4 dB at moderate-to-high SNR (15–20 dB), while differences are small at low SNR and CP can be slightly worse. In DeepMIMO, Tucker is consistently slightly better than CP, indicating greater robustness under model mismatch and richer scattering.
3. **Hybrid tensor–neural architecture:** Tensor-NN achieves 24–44% additional NMSE reduction on DeepMIMO ray-tracing channels relative to pure tensor methods and surpasses the ResNet baseline for $\rho \geq 0.04$, indicating that residual learning captures deviations beyond dominant low-rank structure.
4. **Sample complexity:** Recovery threshold analysis shows that the minimum number of pilot observations scales approximately as $|\Omega|_{\min} \approx C \cdot L(N_r + N_t + N_f)$ rather than the ambient tensor size $N_r N_t N_f$, with empirical oversampling factors $C \approx 11\text{--}41$ exceeding CP-based theoretical minima, in part due to Tucker core parameters and algorithmic suboptimality.

The framework has limitations that warrant future investigation: (i) rank selection remains fixed per experiment rather than data-driven; (ii) high-mobility and time-varying channels are not modeled; (iii) the neural component requires offline training on representative data; and (iv) hardware impairments beyond additive noise are not considered.

Future directions include extension to time-varying channels via higher-order tensor decompositions incorporating temporal modes, reconfigurable intelligent surface (RIS)-aided systems with coupled tensor factors, adaptive rank selection strategies, and integrated sensing and communications (ISAC) scenarios requiring joint channel and target estimation. The proposed structure-informed approach naturally extends to emerging extremely large-scale MIMO (XL-MIMO) regimes, where complexity scaling with effective multilinear rank rather than ambient dimension becomes essential for computational tractability.

References

- [1] T. L. Marzetta, E. G. Larsson, H. Yang, and H. Q. Ngo, *Fundamentals of Massive MIMO*. Cambridge University Press, 2016.
- [2] R. W. Heath, N. Gonzalez-Prelcic, S. Rangan, W. Roh, and A. M. Sayeed, “An overview of signal processing techniques for millimeter wave mimo systems,” *IEEE journal of selected topics in signal processing*, vol. 10, no. 3, pp. 436–453, 2016.
- [3] E. Björnson, J. Hoydis, L. Sanguinetti *et al.*, “Massive mimo networks: Spectral, energy, and hardware efficiency,” *Foundations and Trends in Signal Processing*, vol. 11, no. 3-4, pp. 154–655, 2017.
- [4] E. Björnson, L. Sanguinetti, H. Wymeersch, J. Hoydis, and T. L. Marzetta, “Massive mimo is a reality—what is next?: Five promising research directions for antenna arrays,” *Digital Signal Processing*, vol. 94, pp. 3–20, 2019.
- [5] F. Liu, Y. Cui, C. Masouros, J. Xu, T. X. Han, Y. C. Eldar, and S. Buzzi, “Integrated sensing and communications: Toward dual-functional wireless networks for 6g and beyond,” *IEEE journal on selected areas in communications*, vol. 40, no. 6, pp. 1728–1767, 2022.
- [6] X. Rao and V. K. N. Lau, “Distributed compressive CSIT estimation and feedback for FDD multi-user massive MIMO systems,” *IEEE Transactions on Signal Processing*, vol. 62, no. 12, pp. 3261–3271, 2014.
- [7] A. Alkhateeb, O. El Ayach, G. Leus, and R. W. Heath, “Channel estimation and hybrid precoding for millimeter wave cellular systems,” *IEEE journal of selected topics in signal processing*, vol. 8, no. 5, pp. 831–846, 2014.
- [8] H. He, C.-K. Wen, S. Jin, and G. Y. Li, “Deep learning-based channel estimation for beamspace mmWave massive MIMO systems,” *IEEE Wireless Communications Letters*, vol. 7, no. 5, pp. 852–855, 2018.
- [9] M. Soltani, V. Pober, M. Doroslovacki, and R. M. Buehrer, “Deep learning-based channel estimation,” *IEEE Communications Letters*, vol. 23, no. 4, pp. 652–655, 2019.
- [10] M. Boloursaz Mashhadi and D. Gündüz, “Deep learning for massive MIMO channel state acquisition and feedback,” *Journal of the Indian Institute of Science*, vol. 100, no. 2, pp. 369–382, 2020.
- [11] J. Guo, T. Chen, S. Jin, G. Y. Li, X. Wang, and X. Hou, “Deep learning for joint channel estimation and feedback in massive MIMO systems,” *Digital Communications and Networks*, vol. 10, no. 1, pp. 83–93, 2024.
- [12] J. Gao, C. Zhong, G. Y. Li, and Z. Zhang, “Deep learning-based channel estimation for massive mimo with hybrid transceivers,” *IEEE Transactions on Wireless Communications*, vol. 21, no. 7, pp. 5162–5174, 2021.
- [13] G. E. Karniadakis, I. G. Kevrekidis, L. Lu, P. Perdikaris, S. Wang, and L. Yang, “Physics-informed machine learning,” *Nature Reviews Physics*, vol. 3, no. 6, pp. 422–440, 2021.
- [14] Y. He, N. Xu, L. Cheng, and H. Yuan, “Attention-guided wireless channel modeling and generating,” *Applied Sciences*, vol. 15, no. 6, p. 3058, 2025.

- [15] B. Böck, A. Oeldemann, T. Mayer, F. Rossetto, and W. Utschick, “Physics-informed generative modeling of wireless channels,” *arXiv preprint arXiv:2502.10137*, 2025.
- [16] N. D. Sidiropoulos, L. De Lathauwer, X. Fu, K. Huang, E. E. Papalexakis, and C. Faloutsos, “Tensor decomposition for signal processing and machine learning,” *IEEE Transactions on Signal Processing*, vol. 65, no. 13, pp. 3551–3582, 2017.
- [17] Z. Zhou, J. Fang, L. Yang, H. Li, Z. Chen, and R. S. Blum, “Low-rank tensor decomposition-aided channel estimation for millimeter wave MIMO-OFDM systems,” *IEEE Journal on Selected Areas in Communications*, vol. 35, no. 7, pp. 1524–1538, 2017.
- [18] A. Audy, D. Xia, and M. Yuan, “Tensors in high-dimensional data analysis: Methodological opportunities and theoretical challenges,” *Annual review of statistics and its application*, vol. 12, no. 1, pp. 527–551, 2025.
- [19] D. S. Rocha, G. Favier, and C. A. R. Fernandes, “Closed-form receiver for multi-hop MIMO relay systems with tensor space-time coding,” *Journal of Communication and Information Systems*, vol. 34, no. 1, pp. 50–54, 2019.
- [20] R. Zhang, L. Cheng, S. Wang, Y. Lou, W. Wu, and D. W. K. Ng, “Tensor decomposition-based channel estimation for hybrid mmWave massive MIMO in high-mobility scenarios,” *IEEE Transactions on Communications*, vol. 70, no. 9, pp. 6325–6340, 2022.
- [21] R. W. Heath Jr and A. Lozano, *Foundations of MIMO communication*. Cambridge University Press, 2018.
- [22] E. Candes and B. Recht, “Exact matrix completion via convex optimization,” *Communications of the ACM*, vol. 55, no. 6, pp. 111–119, 2012.
- [23] T. G. Kolda and B. W. Bader, “Tensor decompositions and applications,” *SIAM Review*, vol. 51, no. 3, pp. 455–500, 2009.
- [24] L. De Lathauwer, B. De Moor, and J. Vandewalle, “A multilinear singular value decomposition,” *SIAM Journal on Matrix Analysis and Applications*, vol. 21, no. 4, pp. 1253–1278, 2000.
- [25] K. F. Masood, J. Tong, J. Xi, J. Yuan, Q. Guo, and Y. Yu, “Low-rank matrix sensing-based channel estimation for mmWave and THz hybrid MIMO systems,” *IEEE Journal of Selected Topics in Signal Processing*, vol. 17, no. 4, pp. 777–793, 2023.
- [26] J. Liu, P. Musalski, P. Wonka, and J. Ye, “Tensor completion for estimating missing values in visual data,” *IEEE transactions on pattern analysis and machine intelligence*, vol. 35, no. 1, pp. 208–220, 2012.
- [27] K. Gregor and Y. LeCun, “Learning fast approximations of sparse coding,” in *Proceedings of the 27th International Conference on Machine Learning (ICML)*, 2010, pp. 399–406.
- [28] V. Monga, Y. Li, and Y. C. Eldar, “Algorithm unrolling: Interpretable, efficient deep learning for signal and image processing,” *IEEE Signal Processing Magazine*, vol. 38, no. 2, pp. 18–44, 2021.
- [29] H. He, S. Jin, C.-K. Wen, F. Gao, G. Y. Li, and Z. Xu, “Model-driven deep learning for physical layer communications,” *IEEE Wireless Communications*, vol. 26, no. 5, pp. 77–83, 2019.

- [30] O. Ronneberger, P. Fischer, and T. Brox, “U-net: Convolutional networks for biomedical image segmentation,” in *International Conference on Medical image computing and computer-assisted intervention*. Springer, 2015, pp. 234–241.
- [31] D. P. Kingma and J. Ba, “Adam: A method for stochastic optimization,” in *International Conference on Learning Representations (ICLR)*, 2015. [Online]. Available: <https://arxiv.org/abs/1412.6980>
- [32] A. Paszke, S. Gross, F. Massa, A. Lerer, J. Bradbury, G. Chanan, T. Killeen, Z. Lin, N. Gimelshein, L. Antiga *et al.*, “Pytorch: An imperative style, high-performance deep learning library,” *Advances in neural information processing systems*, vol. 32, 2019.
- [33] E. J. Candès and Y. Plan, “Matrix completion with noise,” *Proceedings of the IEEE*, vol. 98, no. 6, pp. 925–936, 2010.
- [34] A. Alkhateeb, “DeepMIMO: A generic deep learning dataset for millimeter wave and massive MIMO applications,” *arXiv preprint arXiv:1902.06435*, 2019, available: <https://deepmimo.net>.
- [35] K. He, X. Zhang, S. Ren, and J. Sun, “Deep residual learning for image recognition,” in *Proceedings of the IEEE conference on computer vision and pattern recognition*, 2016, pp. 770–778.
- [36] D. Burghal, Y. Li, P. Madadi, Y. Hu, J. Jeon, J. Cho, A. F. Molisch, and J. Zhang, “Enhanced AI-based CSI prediction solutions for massive MIMO in 5G and 6G systems,” *IEEE Access*, vol. 11, pp. 117 810–117 825, 2023.
- [37] P. Barman, V. Dehalwar, and R. Pateriya, “CSI Prediction for 5G and B5G in mMIMO System using Deep Learning Approach,” in *2025 IEEE Future Networks World Forum (FNWF)*. IEEE, 2025, pp. 1–6.
- [38] C. Cai, G. Li, H. V. Poor, and Y. Chen, “Nonconvex low-rank tensor completion from noisy data,” *Advances in neural information processing systems*, vol. 32, 2019.